Implementation of an offset-dipole magnetic field in a geometric pulsar emission code

M Breed[1], C Venter[1], A K Harding[2] and T J Johnson[3]

[1] Centre for Space Research, North-West University, Potchefstroom Campus, Private Bag X6001, Potchefstroom, 2520, South Africa

[2] Astrophysics Science Division, NASA Goddard Space Flight Center, Greenbelt, MD 20771, USA

[3] National Research Council Research Associate, National Academy Of Sciences, Washington, DC 20001, resident at Naval Research Laboratory, Washington, DC 20375, USA

E-mail: 20574266@nwu.ac.za

Abstract. The field of γ-ray pulsars (rapidly spinning and highly magnetized neutron stars; NSs) has been revolutionized by the launch of *Fermi* Large Area Telescope (LAT) in June 2008. *Fermi* LAT has just released its second pulsar catalogue describing the properties of some 117 γ-ray pulsars. The light curves (LCs) of these pulsars show great variety in profile shape, and may be divided into three general profile classes based on the relative phase differences between their radio and γ-ray pulses. Such diversity hints at distinct underlying magnetospheric and/or emission geometries for the individual pulsar classes. Detailed geometric modelling of the radio and γ-ray LCs may therefore provide constraints on the magnetospheric and emission characteristics. We implemented an offset-dipole magnetic field in an existing geometric pulsar modelling code which already includes static and retarded dipole fields. The magnetic field of an NS can undergo distortions due to retardation and asymmetric currents that can shift the NS's polar caps (PCs) by different amounts and directions. In our model, this offset is characterized by a parameter ϵ (with $\epsilon = 0$ corresponding to the static dipole case). We constructed sky maps and LCs for several pulsar parameters and magnetic fields, studying the effect of an offset dipole on the resulting LCs. A standard two-pole caustic (TPC) emission geometry was used. As an application, we compared our model LCs with *Fermi* LAT data for the bright Vela pulsar. We will next infer the most probable configuration based on the *Fermi* LAT data, thereby constraining Vela's magnetic structure and system geometry.

1. Introduction

The first pulsar was discovered in 1967 by Bell and Hewish [1]. Pulsars are identified as compact neutron stars (NSs), formed in supernova explosions, that rotate at tremendous rates, and their magnetospheres contain strong electric, magnetic, and gravitational fields [2]. Pulsars emit radiation across the electromagnetic spectrum, including radio, optical, X-ray and γ-rays [3]. We focus on γ-ray pulsars, specifically the Vela pulsar, which is the brightest persistent GeV source in the γ-ray sky. The Vela pulsar was detected [4] by the *Fermi* Large Area Telescope (LAT) [5], a high-energy (HE) γ-ray telescope that was launched in June 2008. *Fermi* LAT measures γ-rays in the energy range between 20 MeV and 300 GeV. The second *Fermi* pulsar catalogue [6] discussing the properties of 117 γ-ray pulsars has just been released.

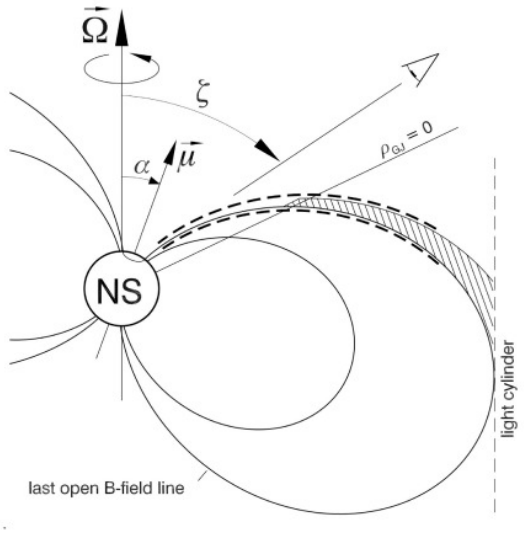

Figure 1. A schematic representation of geometric pulsar models. The TPC emission region extends from $R_{\rm NS}$ (NS radius) up to $R_{\rm LC}$ (light cylinder radius), the OG region from $R_{\rm NCS}$ (null charge surface radius) to $R_{\rm LC}$, and the PSPC from $R_{\rm NS}$ to $R_{\rm LC}$ (covering the full open volume region). Adapted from [7].

2. Model

2.1. Emission gap geometry

Several models have been used to model HE emission from pulsars. These include the two-pole caustic (TPC) [7] (the slot gap (SG) [8] model may be its physical representation), outer gap (OG) [9, 10] and pair-starved polar cap (PSPC) model [11]. Consider the ($\boldsymbol{\Omega}$, $\boldsymbol{\mu}$) plane, with $\boldsymbol{\mu}$ (the magnetic moment) inclined by an angle α with respect to the rotation axis $\boldsymbol{\Omega}$ (the angular velocity). The observer's viewing angle ζ is the angle between the observer's line of sight and the rotation axis. A 'gap region' is defined as the region where particle acceleration and emission take place. The emissivity of HE photons within this gap region is assumed to be uniform in the corotating frame (for the TPC and OG models) and the γ-rays are expected to be emitted tangentially to the local magnetic field in this frame [12], which means that the assumed magnetic field geometry is very important with respect to the predicted light curves (LCs). The gap region for the TPC model extends from the surface of the NS along the entire length of the last closed magnetic field lines, up to the light cylinder (where the corotation speed equals the speed of light), as indicated by the dashed line in Figure 1. For the OG model, the gap region extends from the null-charge surface, where the Goldreich-Julian charge density is $\rho_{\rm GJ} = 0$ [13], to the light cylinder, as indicated by the shaded region (although this emission region may be located at slightly smaller colatitudes compared to the TPC). The PSPC is the gap region that extends from the NS surface to the light cylinder over the full open volume [11]. In what follows, we will focus on the TPC model.

2.2. Magnetic field structure

Several magnetospheric structures have been studied, including the static dipole field [14], the retarded dipole field [15] (a rotating vacuum magnetosphere which can in principle accelerate particles but do not contain any charges or currents) and the force-free field [16] (being filled with charges and currents, but unable to accelerate particles, since the E-field is screened

everywhere). A more realistic pulsar magnetosphere [17] would be one that is intermediate between the retarded and the force-free fields.

The main focus of this paper is on the offset-dipole B-field. Retardation of the B-field and asymmetric currents may cause small distortions in the B-field structure, shifting the PCs by small amounts and different directions. In the 'symmetric case', in the corotating magnetic frame (where $\hat{\mathbf{z}}' \parallel \boldsymbol{\mu}$), the offset-dipole B-field in spherical coordinates is as follows [18]

$$\mathbf{B}'(r', \theta', \phi') = \frac{\mu}{r'^3}\left[\cos\theta'\hat{\mathbf{r}}' + \frac{1}{2}(1+a)\sin\theta'\hat{\boldsymbol{\theta}}' - \epsilon\sin\theta'\cos\theta'\sin(\phi'-\phi_0)\hat{\boldsymbol{\phi}}'\right], \tag{1}$$

where $\mu = B_0 R_{\rm NS}/2$ is the magnetic moment, with B_0 the surface B-field strength at the magnetic pole, $R_{\rm NS}$ the stellar radius, ϕ_0 the magnetic azimuthal angle defining the plane in which the offset occurs, and

$$a = \epsilon\cos(\phi' - \phi_0). \tag{2}$$

The offset is characterized by a parameter ϵ which represents a shift of the PC from the magnetic axis, with $\epsilon = 0$ corresponding to the static-dipole case.

3. Implementation of the offset-dipole B-field in the code

3.1. Transformation of B-field

We implement the offset-dipole B-field by first transforming between spherical and Cartesian coordinate systems, and then rotating the coordinate axes, moving from the magnetic frame to the rotational frame. We generally start with a B-field in the magnetic frame ($\hat{\mathbf{z}}' \parallel \boldsymbol{\mu}$), specified in terms of spherical coordinates

$$\mathbf{B}'(r', \theta', \phi') = B'_r(r', \theta', \phi')\hat{\mathbf{r}}' + B'_\theta(r', \theta', \phi')\hat{\boldsymbol{\theta}}' + B'_\phi(r', \theta', \phi')\hat{\boldsymbol{\phi}}'. \tag{3}$$

This is then transformed to a Cartesian coordinate system:

$$\mathbf{B}'(x', y', z') = B'_x(x', y', z')\hat{\mathbf{x}}' + B'_y(x', y', z')\hat{\mathbf{y}}' + B'_z(x', y', z')\hat{\mathbf{z}}'. \tag{4}$$

This is done using expressions that specify spherical unit vectors and coordinates in terms of Cartesian coordinates (see, e.g., [14]). Next we rotate both the B-field components and its Cartesian frame through an angle $-\alpha$, thereby transforming the B-field from the magnetic frame to the rotational frame ($\hat{\mathbf{z}} \parallel \boldsymbol{\Omega}$):

$$\mathbf{B}(x, y, z) = B_x(x, y, z)\hat{\mathbf{x}} + B_y(x, y, z)\hat{\mathbf{y}} + B_z(x, y, z)\hat{\mathbf{z}}. \tag{5}$$

After initial implementation of the offset-dipole field in the geometric code we discovered that we could solve the PC rim (for details, see [12]) only for small values of the offset parameter ϵ. We improved the range of ϵ by changing the parameters $\theta_{\rm in}$ and $\theta_{\rm out}$, which delimit a bracket in colatitude thought to contain the last open field line (tangent to the $R_{\rm LC}$). Figure 2 indicates the progressively larger range of ϵ that we were able to use upon decreasing $\theta_{\rm in}$ and increasing $\theta_{\rm out}$.

3.2. The offset-dipole E-field

It is important to take the accelerating E-field into account (in a physical model) when such expressions are available, since this will modulate the emissivity in the gap (as opposed to geometric models where we just assume constant emissivity). The low-altitude E-field in the offset-dipole magnetosphere, for the SG model, is given by

$$E_{\parallel,\rm low} \approx -3\mathcal{E}_0\nu_{\rm SG}x^a\left\{\frac{\kappa}{\eta^4}e_{1\rm A}\cos\alpha + \frac{1}{4}\frac{\theta_0^{1+a}}{\eta}\times\left[e_{2\rm A}\cos\phi' + \frac{1}{4}\epsilon\kappa e_{3\rm A}(2\cos\phi_0 - \cos(2\phi'-\phi_0))\right]\sin\alpha\right\}(1-\xi_*^2), \tag{6}$$

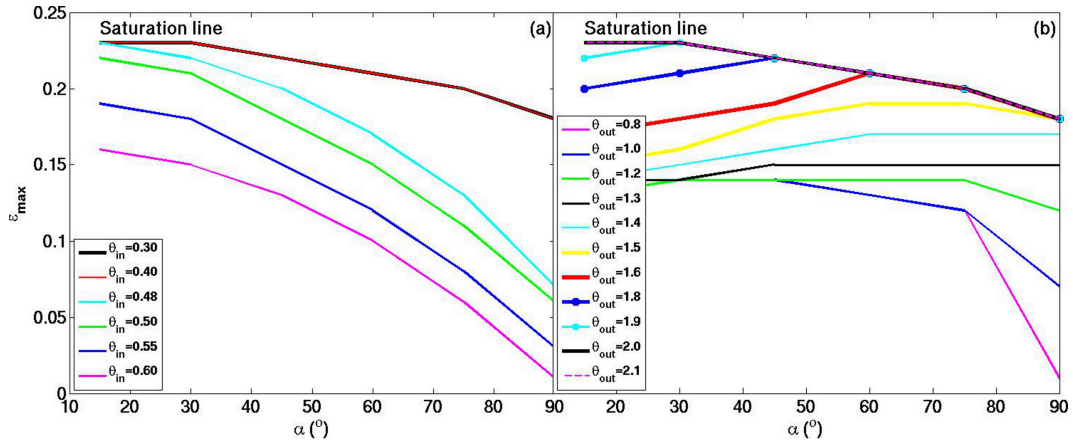

Figure 2. A plot of $\epsilon_{\rm max}$ as a function of α. In panel (a) each line corresponds to a different value of $\theta_{\rm in}$ (in radians) for a constant value of $\theta_{\rm out} = 2.0$ radians. For values smaller than $\theta_{\rm in} = 0.40$, $\epsilon_{\rm max}$ becomes saturated, and for larger $\theta_{\rm in}$, $\epsilon_{\rm max}$ decreases significantly. In panel (b) each line corresponds to a different value of $\theta_{\rm out}$ for a constant value of $\theta_{\rm in} = 0.3$, where $\epsilon_{\rm max}$ becomes saturated at $\theta_{\rm out} = 2.0$, and as $\theta_{\rm out}$ decreases, $\epsilon_{\rm max}$ also decreases.

where the symbols have the same meaning as in [19]. Here

$$e_{1A} = 1 + \frac{a}{3}(\eta^3 - 1); \quad e_{2A} = (1+3a)\eta^{(1+a)/2} - 2a; \quad e_{3A} = \frac{5-3a}{\eta^{(5-a)/2}} + 2a. \tag{7}$$

We approximate the high-altitude SG E-field by [19]

$$E_{\parallel,\rm high} \approx -\frac{3}{8}\left(\frac{\Omega R}{c}\right)^3 \frac{B_0}{f(1)}\nu_{\rm SG}x^a \left\{\left[1 + \frac{1}{3}\kappa\left(5 - \frac{8}{\eta_c^3}\right) + 2\frac{\eta}{\eta_{\rm LC}}\right] \times \cos\alpha + \frac{3}{2}\theta_0 H(1)\sin\alpha\cos\phi'\right\}(1-\xi_*^2), \tag{8}$$

and the total E-field by

$$E_{\parallel,\rm SG} \simeq E_{\parallel,\rm low}\exp\left(\frac{-(\eta-1)}{(\eta_c-1)}\right) + E_{\parallel,\rm high}, \tag{9}$$

where $\eta_c = r_c/R_{\rm NS}$ is the critical scaled radius where the high-altitude and low-altitude E-field solutions are matched.

4. Results

4.1. Solution of particle equation of motion

Using equation (9) we next solve the particle transport equation (taking only curvature losses into account)

$$\dot{\gamma} = \dot{\gamma}_{\rm gain} + \dot{\gamma}_{\rm loss} = \frac{eE_\parallel}{mc} - \frac{2e^2\gamma^4}{3\rho_{\rm curv}^2 mc} \tag{10}$$

to obtain the particle Lorentz factor $\gamma(\eta, \phi', \xi_*)$. Radiation reaction occurs when the energy gain balances the loss, and $\dot{\gamma} = 0$. In Figure 3 we plot the $\log_{10}$ of curvature radius $\rho_{\rm curv}$, total E-field, gain rate $\dot{\gamma}_{\rm gain}$, loss rate $\dot{\gamma}_{\rm loss}$, and particle Lorentz factor γ as a function of normalized radial distance $r/R_{\rm LC}$. We can see that the radiation reaction limit is not reached in this case, due to the relatively low SG E-field. The Lorentz factor is initially set to $\gamma = 100$ and rapidly

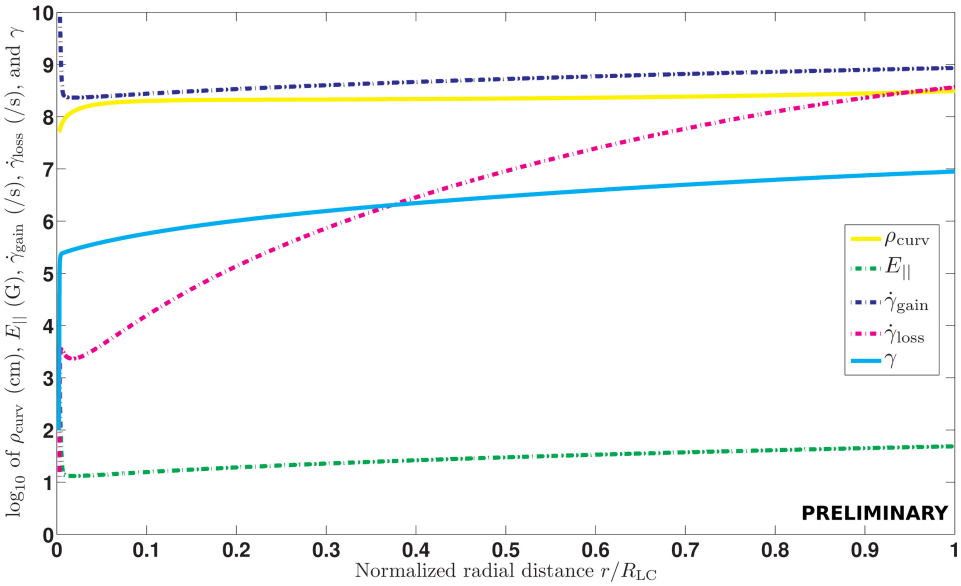

Figure 3. Plot of $\log_{10}$ of curvature radius $\rho_{\rm curv}$ (solid yellow line), total E-field (dash-dotted green line), gain (acceleration) rate $\dot{\gamma}_{\rm gain}$ (dash-dotted dark blue line), loss rate $\dot{\gamma}_{\rm loss}$ (dash-dotted pink line), and the Lorentz factor γ (solid light blue line) as a function of normalized radial distance $r/R_{\rm LC}$. We used $P = 0.0893$ s, $B_0 = 1.05 \times 10^{13}$ G (GR-corrected B-field), $I = 0.4MR_{\rm NS}^2 = 1.14 \times 10^{45}$ g cm^2, $\phi' = 1.60$ radians (at the surface), $\xi_* = 0$, and $\eta_c = 1.4$.

rises until it nearly reaches $\gamma \sim 10^7$. For different choices of ϕ' and ξ_*, the E-field may be even lower and γ may not even exceed $\sim 10^5$, leading to negligible curvature radiation losses along those field lines. On 'unfavourably curved' field lines, the E-field may even change sign at higher altitudes. This may cause oscillation of particles and very low values of γ, and such field lines should be ignored when constructing phaseplots.

4.2. Phaseplots and LCs

In Figure 4, we show the phaseplots (emission per solid angle in ζ and $\phi_{\rm L}$ bins) and their corresponding LCs (i.e., cuts along constant ζ) for the offset-dipole B-field and TPC model. The dark circle in panel (a) is the non-emitting PC, and the sharp, bright regions are the emission caustics, where radiation is bunched in phase due to relativistic effects. The caustic structure is qualitatively different between the two cases (constant emissivity vs. solution of γ using $E_\parallel$), leading to differences in the resulting LCs. The caustics seem wider and more pronounced in the constant-emissivity case. Note that these LCs are merely representative, and still fail to adequately reproduce the second peak in the measured profile.

5. Conclusions and future work

We have studied the effect of implementing the offset-dipole B-field on γ-ray LCs for the TPC geometry. We observe that the PC is indeed offset compared to the case of the static dipole (not shown Figure 4) when assuming a constant emissivity. However, when including an E-field and solving for γ, we see that the resulting phaseplot becomes qualitatively different, given the fact that γ only becomes large enough to yield significant curvature radiation at large altitudes. Furthermore, we do not attain the radiation-reaction limit, due to a relatively low E-field. In future, we want to continue to extend the range of ϵ for which we are able to solve the PC rim.

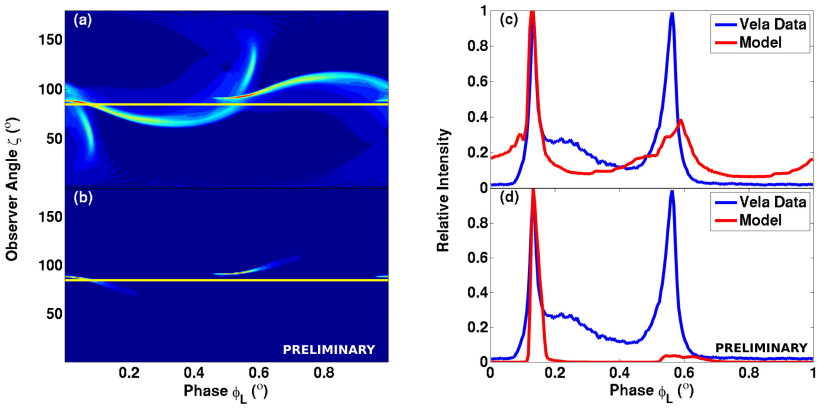

Figure 4. Phaseplots and LCs for the offset-dipole field. Panels (a) and (b) illustrate phaseplots for $\alpha = 60°$ and panels (c) and (d) their corresponding LCs for $\zeta = 85°$. The solid blue line denotes the observed Vela profile (e.g., [20]) and the solid red line our model. Panel (a) and (c) are for the case of constant emissivity, whereas panel (b) and (d) are for the case when using the offset-dipole E-field and solving for γ. We assumed $\epsilon = 0.2$, a gap width of 5% of the PC angle, and $R_{\rm max} = 1.2R_{\rm LC}$ for an SG model.

We also want to solve for η_c on each field line, instead of using a constant value where we match E-field solutions, and we need to improve our handling of field lines where $E_{\parallel}$ changes sign with altitude. Lastly, we want to produce LCs for several model parameters and search for a best-fit profile, thereby constraining Vela's low-altitude magnetic structure and system geometry.

Acknowledgments

This work is supported by the South African National Research Foundation (NRF). AKH acknowledges the support from the NASA Astrophysics Theory Program. CV, TJJ, and AKH acknowledge support from the *Fermi* Guest Investigator Program.

References

[1] Hewish A *et al.* 1968 *Nature* **217** 709
[2] Abdo A A *et al.* 2010 *ApJ* **187** 460
[3] Becker W, Gil J A and Rudak B 2007 *Highlights of Astronomy* **14** 109
[4] Abdo A A *et al.* 2009 *ApJ* **696** 1084
[5] Atwood W B *et al.* 2009 *ApJ* **697** 1071
[6] Abdo A A *et al.* 2013 *ApJ*, accepted (arXiv:1305.4385)
[7] Dyks J and Rudak B 2003 *ApJ* **598** 1201
[8] Muslimov A G and Harding A K 2003 *ApJ* **588** 430
[9] Cheng K S, Ho C and Ruderman M 1986, *ApJ* **300** 500
[10] Romani R W 1996 *ApJ* **470** 469
[11] Harding A K, Usov V V and Muslimov A G 2005 *ApJ* **622** 531
[12] Dyks J, Harding A K and Rudak B 2004 *ApJ* **606** 1125
[13] Goldreich P and Julian W H 1969 *ApJ* **157** 869
[14] Griffiths D J 1995 *Introduction to Electrodynamics* (San Francisco: Pearson Benjamin Cummings)
[15] Deutsch A J 1955 *Annales d'Astrophysique* **18** 1
[16] Contopoulos I, Kazanas D and Fendt C 1999 *ApJ* **511** 351
[17] Kalapotharakos C, Kazanas D, Harding A and Contopoulos I 2012 *ApJ* **749** 2
[18] Harding A K and Muslimov A G 2011 *ApJ* **743** 181
[19] Muslimov A G and Harding A K 2004 *ApJ* **606** 1143
[20] Abdo A A *et al.* 2010b *ApJ* **713** 154